ARTICLE

Bidirectional Synaptic Phototransistor Based on Two-Dimensional Ferroelectric Semiconductor for Mixed Color Pattern Recognition

Yitong Chen, Min Zhang, Dingwei Li, Yingjie Tang, Huihui Ren, Jiye Li, Kun Liang, Yan Wang, Liaoyong Wen, Wenbin Li, Wei Kong, Shi Liu, Hong Wang, Donglin Wang, and Bowen Zhu*

Read Online

ACCESS | Metrics & More | Article Recommendations | Supporting Information

ABSTRACT: Optoelectronic synaptic devices capable of processing multiwavelength inputs are critical for neuromorphic vision hardware, which remains an important challenge. Here, we develop a bidirectional synaptic phototransistor based on a two-dimensional ferroelectric semiconductor of α-In$_2$Se$_3$, which exhibits bidirectional potentiated and depressed synaptic weight update under optical pulse stimulation. Importantly, the bidirectional optoelectronic synaptic behavior can be extended to multiwavelengths (blue, green, and red light), which could be used for color recognition. The mechanism underlying the bidirectional synaptic characteristics is attributed to the gate-configurable barrier heights as revealed by the Kelvin probe force microscopy measurement. The α-In$_2$Se$_3$ device exhibits

versatile synaptic plasticity such as paired-pulse facilitation, short- and long-term potentiation, and long-term depression. The bidirectional optoelectronic synaptic weight updates under multiwavelength inputs enable a high accuracy of 97% for mixed color pattern recognition.

KEYWORDS: two-dimensional materials, α-In$_2$Se$_3$, phototransistor, optoelectronics, bidirectional photoresponse
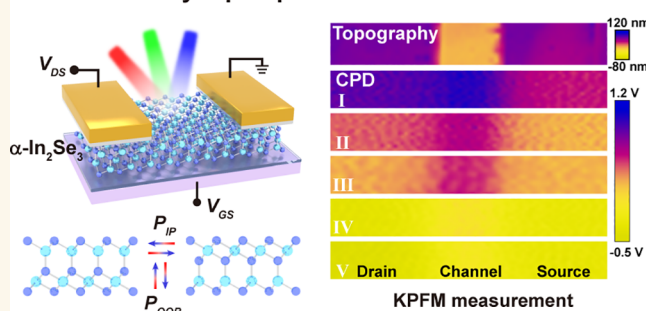
Neuromorphic computing has emerged as an innovative approach with the feature of massive parallelism and high energy efficiency potentially breaking the von Neumann bottleneck.[1−4] Inspired by the human vision system, optoelectronic synaptic devices have drawn extensive interest in visual information recognition and data processing for building artificial vision systems.[5−9] Various optoelectronic synaptic devices have been explored to emulate the biological synaptic potentiation and depression characteristics, enabling conductance state changes in response to optical intensity to enhance image recognition.[10−12] However, the reported device conductance changes are mainly driven by the hybrid combination of optical excitatory and electrical inhibitory pulses, resulting in computational latency that makes it challenging to recognize and distinguish various colors.[13−17] Notably, the realization of optical-stimulated depressed synaptic weight updates required for accurate interpretation and mixed-color visual information recognition have remained scarce.

Various optical-stimulated synapses have been proposed to achieve long-term potentiation and depression (LTP/LTD) characteristics—through both optical pulse stimulation. For example, negative synaptic weight updates have been demonstrated in black phosphorus (BP) by forming oxidation-related defects and creating charge traps.[18−21] Semiconductor heterostructures have been employed to realize bidirectional synaptic modulation, exploiting the carriers trapping and detrapping at the heterointerface.[22−29] Despite these advances, the environmental instability of BP leads to the degradation of device performance, and heterostructures struggle to achieve fine control of synaptic weight due to
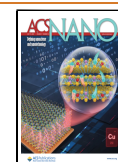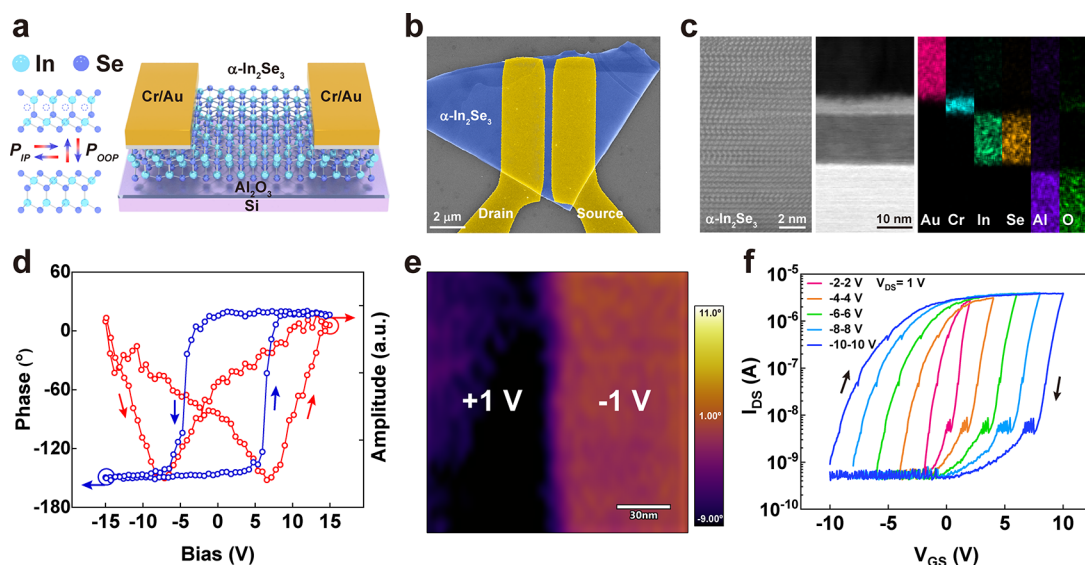
Figure 1. Structure and electrical performance of optoelectronic transistor based on α-In$_2$Se$_3$. (a) The schematic diagram of the crystal structure of 2H α-In$_2$Se$_3$ with different out-of-plane (OOP) and in-plane (IP) polarization (left panel). Schematic illustration of the optoelectronic transistor. Ferroelectric semiconductor α-In$_2$Se$_3$ used as channel material, with electron-beam lithographically defined source and drain electrode regions (right panel). (b) False-color SEM image of the device, scale bar: 2 μm. (c) High-angle annular dark-field-scanning transmission electron microscope (HAADF-STEM) image of the α-In$_2$Se$_3$ in the device (scale bar: 2 nm, left panel), and large-scale cross-sectional TEM image (middle panel) and the corresponding chemical distribution of elements gold (Au), chromium (Cr), indium (In), selenium (Se), aluminum (Al), and oxygen (O) (scale bar: 10 nm, right panel). (d) Off-field PFM amplitude hysteresis loops (red trace) and phase hysteresis (blue trace) of 60 nm thick sample on Au-coated Si substrate, showing clear ferroelectric polarization switching. (e) PFM phase image after poling with $\pm$1 V, scale bar: 30 nm. (f) Transfer characteristics at various gate voltage range under dark ambient condition (V_{DS} = 1 V). The current fluctuations in backward V_{GS} sweeping could be attributed to slow response of the electrical testing system during sharp current decrease.

metastable traps, overshadowing their further applications. In this regard, the emerging two-dimensional (2D) ferroelectric semiconductor α-In$_2$Se$_3$, with its coupled ferroelectric and semiconductor properties and appropriate bandgap for photosensing, appears to be a superior candidate for multifunctional optoelectronics.[30−38] Despite optoelectronic synaptic capabilities that have been demonstrated in α-In$_2$Se$_3$-based devices, the optical pulse stimulation only induced potentiated synaptic weight update, rendering them less advantageous in artificial vision systems.[39−41]

Here, we report an optically stimulated bidirectional synaptic phototransistor based on the 2D ferroelectric semiconductor of α-In$_2$Se$_3$. The bidirectional optoelectronic LTP/LTD synaptic weight updates and fine-tunable synaptic characteristics are achieved. Kelvin probe force microscopy (KPFM) measurements were performed to reveal that the underlying mechanism of bidirectional synaptic weight update could be attributed to the configurable barrier heights via gate-modulated ferroelectric polarization switching in α-In$_2$Se$_3$. The device can also mimic versatile synaptic functions, including paired-pulse facilitation (PPF), short-term/long-term potentiation (STP/LTP), the transition from STP to LTP, and learning-forgetting behaviors. The singular potentiated and depressed synaptic weight updates were obtained for three distinct wavelengths: blue (450 nm), green (520 nm), and red (675 nm), showing promise in complex mixed color pattern recognition. As a demonstration, the α-In$_2$Se$_3$-based optoelectronic synapse reached exceptionally high accuracies of 97% for the mixed color pattern recognition in a simulated neural network. This demonstration of a single-channel device with optically configurable capabilities shows considerable promise for power-efficient artificial vision systems.

RESULTS AND DISCUSSION

Device Design and Characterization. The emerging 2D ferroelectric semiconductor α-In$_2$Se$_3$, with coupled ferroelectric and semiconductor characteristics as well as the electrically configurable interlocked out-of-plane (OOP) and in-plane (IP) polarization switching properties, is promising for neuromorphic computing applications.[42−47] Each monolayer α-In$_2$Se$_3$ is arranged in the order of Se-In-Se-In-Se; the movement of central Se atom can reverse the orientation of the crystal structure of α-In$_2$Se$_3$, causing the lock-in polarization of OOP and IP, and lead to the robust existence of intrinsic ferroelectricity (Figure 1a, left panel).[48,49] We employed α-In$_2$Se$_3$ as the channel material, a heavily boron-doped Si substrate as the back-gate electrode, Al$_2$O$_3$ as the gate dielectric, and Cr/Au as source/drain electrodes (Figure 1a, right panel). The high quality of the exfoliated and transferred 2H α-In$_2$Se$_3$ in the fabricated devices was demonstrated by Raman spectroscopy and X-ray diffraction (XRD) characterization (Figure S1).[50] The false-color scanning electron microscopy (SEM) image of the as-fabricated device is shown in Figure 1b. Detailed device fabrication can be found in the Experimental Section. The device cross-section was observed by transmission electron microscope (TEM), and the corresponding energy-dispersive X-ray spectroscopy (EDS) element mapping is displayed in Figure 1c.

We investigated the ferroelectric properties of α-In$_2$Se$_3$ in piezoelectric force microscopy (PFM) measurements; a locally ferroelectric hysteresis loop can be obtained in switching spectroscopy mode (SS-PFM) by applying a dc bias to tune and measure the response at zero dc bias each time.[51,52] The distinct phase and amplitude hysteresis loops demonstrate the intrinsic ferroelectric behavior of α-In$_2$Se$_3$ (Figure 1d).
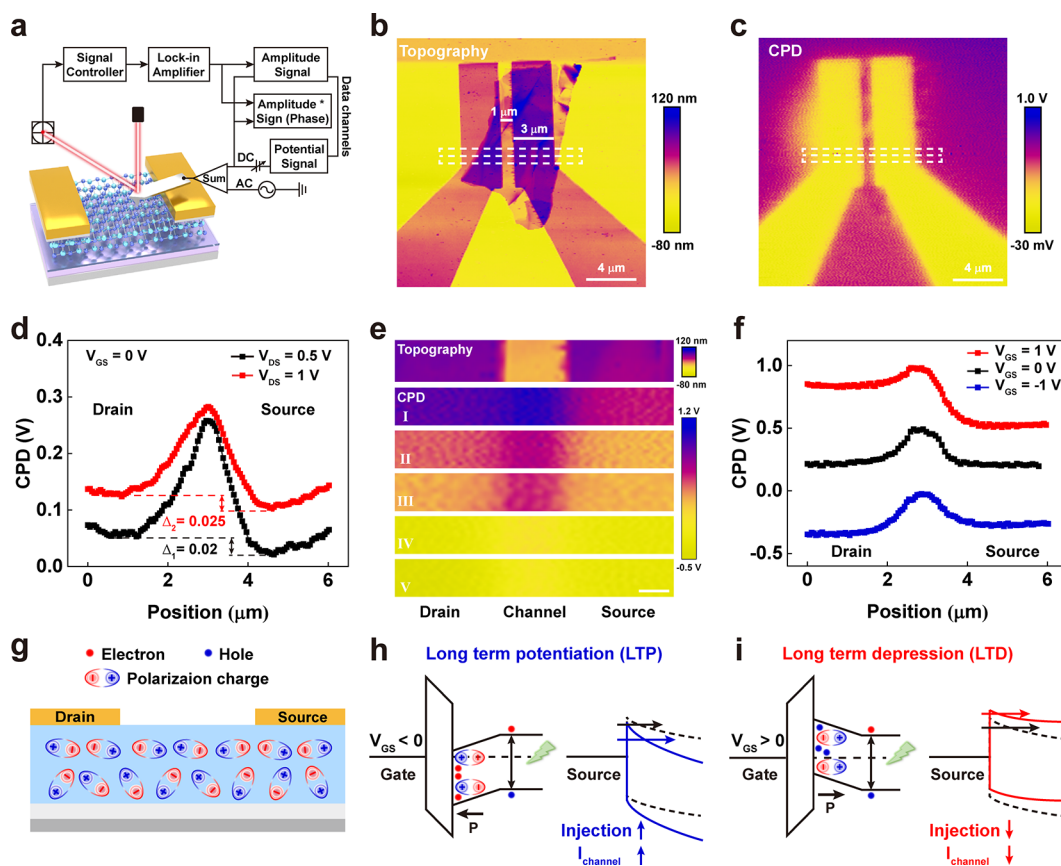
Figure 2. KPFM measurement of the device. (a) Schematic illustration of the *in situ* KPFM measurement for α-In$_2$Se$_3$ FET. (b) AFM topography image of the as-prepared device, scale bar: 4 μm. (c) Contact potential difference (CPD) mapping of the as-prepared device without external voltage. (d) CPD profile of the as-prepared device under $V_{DS} = 0.5$ and $V_{DS} = 1$ when $V_{GS} = 0$ V. (e) Partial topography image (top panel) without external bias, and contact potential difference (CPD) mapping (I−V) of the device at different states (I: $V_{GS} = 1$ V, II: $V_{GS} = 0.5$ V, III: without external bias, IV: $V_{GS} = -0.5$ V, V: $V_{GS} = -1$ V, fixed $V_{DS} = 0.5$ V unless other specify). Scale bar: 500 nm. (f) CPD profile across the device under different gate voltages with $V_{DS} = 0.5$ V deviated from (e). (g) Schematic illustration of spontaneous polarization charge at dark ambient condition without external bias. (h,i) Energy band diagrams of the synaptic weight update process of long-term potentiation and depression (LTP/D) with optical pulse stimulation. The black arrows point out the polarization direction of α-In$_2$Se$_3$.

Furthermore, the electrical configurability of α-In$_2$Se$_3$ was carefully tested after the ferroelectric domain patterning by applying a bias of ±1 V. The clear contrast between regions and domain boundaries can be observed in the PFM phase and amplitude mapping, demonstrating the electrically reversible switching of ferroelectric polarization in α-In$_2$Se$_3$ (Figure 1e and Figure S2). The electrical characteristics of the phototransistor were measured at different sweeping ranges of bottom-gate voltage; by increasing the V_{GS} sweeping range, the hysteresis loops became larger, which is mainly caused by ferroelectric polarization switching (Figure 1f). In the bottom-gate configuration, the application of a negative gate voltage leads to the accumulation of positive polarization charges and electrons, resulting in a low resistance state. Conversely, a positive gate voltage distribution of negative polarization charges and holes indicates a high resistance state. Devices made from mechanically exfoliated α-In$_2$Se$_3$ flakes with a thickness in the range of 10−50 nm showed similar electrical characteristics (Figure S3). In addition, the I_{DS}-V_{DS} characteristic at different gate voltages in the dark ambient conditions is presented in Figure S4.

KPFM Measurements of α-In$_2$Se$_3$ Phototransistor. The coupled ferroelectric and semiconductor characteristics of α-In$_2$Se$_3$ are critical to analyzing and understanding the working

principle with different polarities on device performance, but the interlocked ferroelectric polarization charge has not been well-elucidated yet.[49] To gain insight into the movement of charge carriers with electrically configurable polarization and the modulation of optoelectronic function, we performed Kelvin probe force microscopy (KPFM) measurements on the device. KPFM has emerged as an effective method of achieving the synchronous mapping of the topography and local contact potential difference (CPD) between tip and sample with nanometer resolution (Figure S5).[53] We fixed the as-prepared device on a large substrate and led the electrodes out through wire bonding, allowing us to apply bias to the three electrodes (Figure S6). Additionally, the open device structure without passivation gives us direct access to the surface potential in the channel and the semiconductor-electrode interface regions; thus, we can explore the electrically modulated polarization charge distribution of the device under various operating conditions (Figure 2a). Assuming the work function of the tip remains constant during the measurements, the CPD mapping and line profile reflect the surface electric potential. The topography and CPD on the device without an external electric field were investigated, and there was no relative difference in CPD of source and drain regions (Figure 2b,c). The extracted topography and CPD profiles are presented in Figure S7.
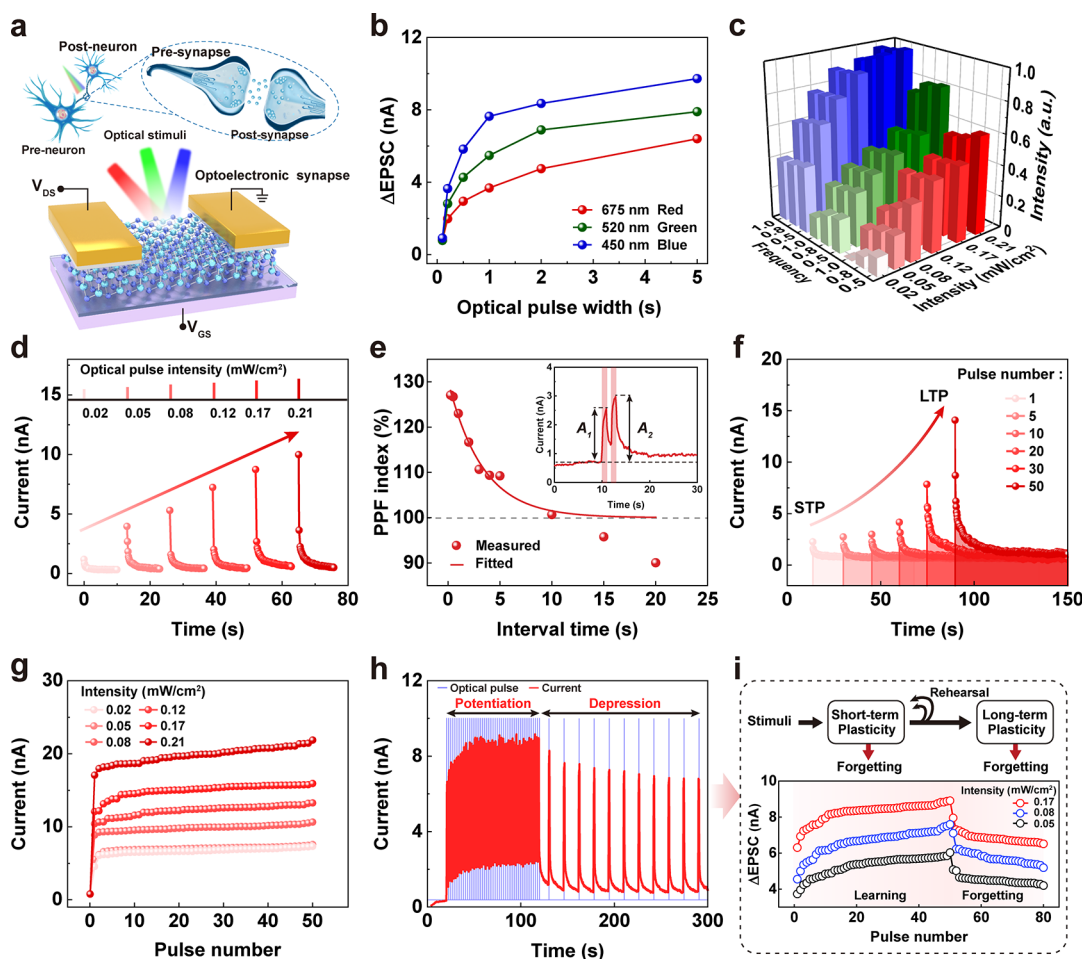
Figure 3. Optical-stimulated characteristics in α-In$_2$Se$_3$ synaptic phototransistor. (a) Schematic illustration of biological neurons and synapses and synaptic phototransistor. (b) The changes of excitatory PSC (ΔEPSC) under optical pulse (red, green, and blue) with different pulse widths (pulse intensity: 0.02 mW/cm^2). (c) Comparison of the relative intensity of ΔEPSC depends on optical intensity and frequency of red, green, and blue optical pulses. (d−i) Optical-stimulated synaptic characteristics at a wavelength of 675 nm, red light. (d) Comparison of the PSC excited by an optical pulse and light intensity ranging from 0.02 to 0.21 mW/cm^2 for 1 s, showing optical-intensity-dependent STP. (e) The PPF characteristic emulated by two optical pulses with a fixed intensity of 0.02 mW/cm^2 and different intervals. The inset shows the PSC triggered by two successive optical pulses. (f) Peak current responses and relaxation time curves under different optical pulse numbers with fixed optical pulse intensity of 0.21 mW/cm^2, pulse width of 1 s, and pulse frequency of 0.5 Hz. (g) Gradual PSC modulation under 50 successive optical pulses training with different intensities (pulse width: 1 s; pulse frequency: 0.5 Hz). (h) Demonstration of facilitation and depression behavior by tuning the interval times of optical pulses. The PSC responses (red curve) to a series of optical pulses with intervals of 1 and 15 s, 1 s duration, and 0.05 mW/cm^2. (i) Schematic diagram of the principle of biological consolidation in the human brain. And the emulation of learning-forgetting behavior with facilitation and depression characteristics by optical pulses (pulse width: 1 s).

Particularly, the metal-semiconductor interface has a lower potential than the α-In$_2$Se$_3$ region, corresponding to the higher work function in the metal-semiconductor interface than the channel region.

Then, we explored the effect of different V_{DS} values (V_{DS} = 0.5 or 1 V) without applied V_{GS} on device performance (Figure 2d). Particularly, the modulation of V_{DS} had only a minor effect on the CPD profile, indicating that the applied V_{DS} does not significantly modulate the built-in potential caused by the IP ferroelectric polarization charge. Consequently, this indicates that the alterations occurring in the polarization charges are not prominently influenced by the applied V_{DS}. Figure 2e presents the selected area topography image and the corresponding CPD mappings (from I to V) with V_{GS} ranging from 1, 0.5, 0, −0.5, and −1 V and fixed V_{DS} = 0.5 V (except for III where V_{GS} = V_{DS} = 0 V), suggesting distinct CPD induced by applied V_{GS} bias. The distinct distribution of CPD under the small V_{GS} within ±1 V allows for insights into the

polarization charge transform process. Under negative V_{GS} (−1 V), we observed an obvious decrease in CPD, and the CPD value of the drain terminal is slightly lower than that of the source terminal under the application of fixed V_{DS} (Figure 2f, Figure S8a). On the other hand, the CPD value increases apparently under positive V_{GS} (1 V) and becomes evidently larger at the drain terminal (Figure 2f, Figure S8b). We attribute the distinct difference of the CPD value between the drain and source terminal to the modulation of the IP polarization charges due to different polarities of the OOP polarization under the V_{GS} configuration and the polarization charge locked in a specific orientation as shown in Figure S9. In addition, the larger energy barrier difference ($e\Delta$CPD) under positive V_{GS} would impede electrons from the interface to the channel region. This tunable barrier variation *via* configurable interlocked polarization in α-In$_2$Se$_3$ can be exploited to realize synaptic behavior.

The α-In$_2$Se$_3$ synaptic phototransistor operates differently from conventional bidirectional synaptic devices, relying on defects and/or charge trapping/detrapping, mainly due to its gate-configured barrier height arising from polarization switching. Schematic illustrations elucidating the mechanism related to the behavior of the charge carriers in the α-In$_2$Se$_3$ synaptic phototransistor are presented (Figure 2g-i). In dark conditions, α-In$_2$Se$_3$ exhibits spontaneous polarization in the absence of an external electric field. Under illumination with negative weight control voltage ($V_{GS} < 0$), the applied V_{GS} across the channel causes downward polarization (P down) and the accumulation of electrons at the semiconductor-dielectric interface (Figure 2g). The reduced tunneling width at the channel-source junction results in more carrier injection (increased channel conductance = potentiation; Figure 2h). Conversely, for the scenario under illumination with positive weight control voltage ($V_{GS} < 0$, P up), the semiconductor-dielectric interface will be cumulated by the number of holes, shielding the effect of the effective gate electric field, resulting in a more pronounced reduction in the channel current. And the increased tunneling width at the α-In$_2$Se$_3$-source junction results in less carrier injection (decreased channel conductance = depression; Figure 2i). The intrinsic ferroelectric properties of α-In$_2$Se$_3$ provide an optically stimulated pathway to emulate both potentiated and depressed characteristics under the same input wavelength.

Optical-Stimulated Synaptic Characteristics. Figure 3a presents a schematic diagram of a synapse, which can act as a communication channel between two neurons to transmit various signal stimuli of different intensities from presynapse to postsynapse *via* neurotransmitters, exhibiting potentiated or depressed responses. The optoelectronic synapse is inspired by the biological synapse in the visual cortex of the brain, which is regarded as the basis of learning and external signal processing. In the optoelectronic synapse based on the α-In$_2$Se$_3$ phototransistor, the gate terminal can act as the weight control terminal to modulate the polarity of α-In$_2$Se$_3$, the external optical pulse stimulation acts as presynaptic signals, and the postsynaptic current (PSC, I_{DS}) can be obtained from the α-In$_2$Se$_3$ channel.

We first explored the PSC responses when optical pulses were applied under a negative weight control voltage ($V_{GS} = -10$ V) and maintained $V_{DS} = 0.1$ V. The changes of excitatory PSC (ΔEPSC) of a separated device as a function of pulse width under red, green, and blue optical pulses are shown in Figure 3b. The enhancement of current is due to the increase of photogenerated charge carriers with prolonged illumination time. We also investigated the effect of pulse intensity and frequency of different wavelength optical pulses (Figure 3c), and the photoresponsivity of this visible light enables us to explore the synaptic functions under the optical pulses of various wavelengths. Figure 3d shows the short-term potentiation (STP) under red optical pulse stimulation with intensities ranging from 0.02 to 0.21 mW/cm^2. Measurements were also performed by using green and blue optical pulses, showing comparable behaviors (Figures S10 & S11). The device exhibits STP with enhanced postsynaptic current with an increase in light intensity, which can be attributed to the generation of photocarriers under illumination, resulting in an increase in current, followed by a decay process toward to the initial state. The decay process can be well-fitted with a double exponential decay function, indicating the existence of a fast and a slow decay mechanism corresponding to intrinsic

photoconduction mechanism and slow traps, respectively. Detailed fitting and analysis information is presented in Figure S12. The effect of paired-pulse facilitation (PPF) was demonstrated by applying two closely red optical pulses with different pulse intervals (Figure 3e inset). Detailed PPF fitting can be found in the Experimental Methods. The calculated PPF index was 127% for $\Delta t = 0.25$ s, and it decreased exponentially to 101% for $\Delta t = 10$ s, suggesting that the learning effect in our device can be enhanced when triggered with repeated optical training pulses (Figure 3e). In the biological synapse, the transition from STP to long-term potentiation (LTP) can be achieved by utilizing repeated pulse stimuli that constantly increase the synaptic weight. The peak current responses and relaxation time curves under different pulse numbers are presented in Figure 3f. As the optical pulse number increased from 1 to 50, the cumulative effect became more pronounced, leading to a higher excitatory PSC response. The accumulation of a progressively higher number of photogenerated carriers that do not dissipate promptly hinders the device's ability to return to its initial state quickly, resulting in the transition from STP to LTP. We further applied 50 consecutive optical pulses of different intensities, and as the number of pulses increased, the current gradually increased due to the generation of more photogenerated charge carriers (Figure 3g).

Interestingly, it can be observed that the PPF index value under red optical pulses for $\Delta t = 15$ and 20 s are lower than 100%, which could not be consistent with the fitted curve, indicating the depressed behavior of the device, which is consistent with the reported device.[54] Taking advantage of this discrepancy in the PPF characteristic of red optical pulse, synaptic plasticity can be potentiated or depressed under appropriate optical pulse stimulation, outperforming the common configuration in optoelectronic synapses where optical and electrical inputs are used for potentiation and depression, respectively. Figure 3h illustrates the application of optical pulses with different time intervals to regulate the synaptic function from facilitation to depression, exhibiting potentiation under 50 high-frequency successive optical stimuli of 1 s intervals, followed by depression by increasing the intervals to 15 s. This conversion can also mimic the principle of biological consolidation in the human brain (Figure 3i). By rationally designing the pulse intervals, the PSC enhancement can be altered under illumination with different intensities to simulate this neuromorphic behavior involving learning-forgetting ability. In comparison, this tuning ability cannot be performed under green and blue optical pulses with the same intensities, and the PPF index value is still in good agreement with the fitted curve despite the increased time intervals (>10 s) (Figures S10b & S11b), possibly due to the relatively low excitation energy of red optical pulse.

Bidirectional Synaptic Weight Updates in α-In$_2$Se$_3$ Synaptic Phototransistor. Achieving mixed-color pattern recognition in synaptic phototransistors requires multiwavelength stimulated potentiated and depressed synaptic weight update in the training process of a neural network. As demonstrated in KPFM measurements, the modulation of polarization switching can be used to realize the configuration of barrier height to achieve an increased or decreased conductance state update. To ensure the feasibility of the optical-stimulated bidirectional synaptic function with different polarization states of α-In$_2$Se$_3$ device, further measurements were made by applying various weight control voltages (V_{GS})
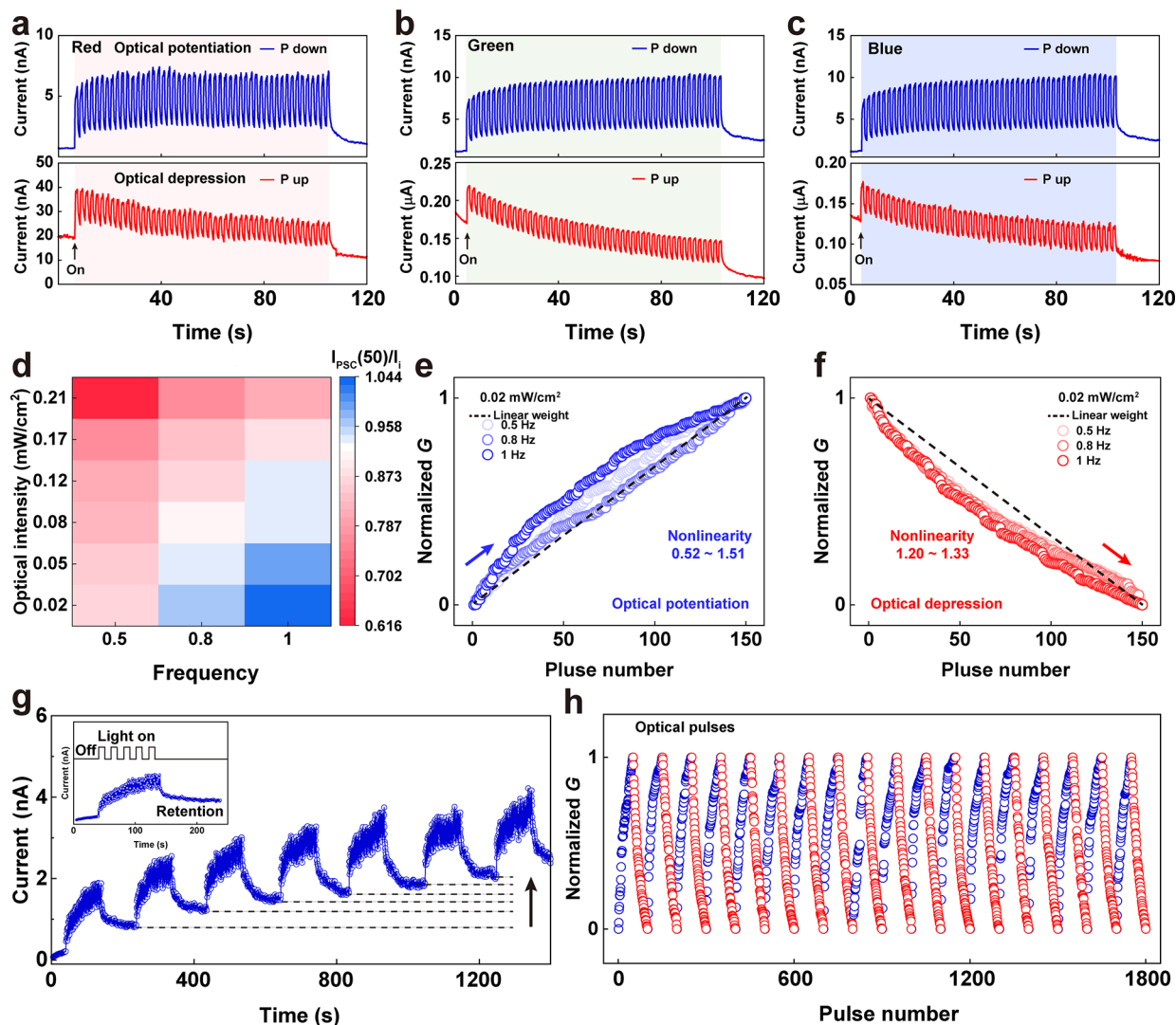
Figure 4. Bidirectional potentiated and depressed synaptic weight updates with respect to various polarity conditions. (a-c) Demonstration of α-In$_2$Se$_3$ synaptic phototransistor where excitation of 50 consecutive optical pulse stimuli with wavelengths of (a) 675 nm (red), (b) 520 nm (green), and (c) 450 nm (blue) induces potentiation and depression. (P down: V_{GS} = −10 V, P up: V_{GS} = 10 V, V_{DS} = 0.1 V. Optical pulse amplitude: 0.02 mW/cm^2, pulse width: 1 s, pulse frequency: 0.5 Hz). (d) The current change ratio of postsynaptic current at the 50th optical pulse (I_{PSC}(50)) to the initial PSC (I_i), which is expressed as I_{PSC}(50)/I_i. (e,f) Normalized conductance (G) of 150 potentiated (e) and 150 depressed (f) synaptic weight update under different optical pulse frequency, including the number representing the fitting nonlinearity (Optical pulse amplitude: 0.02 mW/cm^2). (g) The multistage conductance switching under consecutive 100 optical pulses and the interval of 100 s. The inset shows the first cycle PSC response triggered by 100 optical pulses and the retention characteristic without illumination. (V_{GS} = −10 V, P down. Red light, 0.02 mW/cm^2; pulse width: 1 s; pulse frequency: 0.5 Hz). (h) The normalized conductance change of the LTP/D curves with 18 cycles, where one cycle consists of 50 potentiated responses and 50 depressed synaptic weight updates.

to alter the polarities. The photocurrent increased for each incident optical pulse at negative weight control voltage (V_{GS} = −10 V, P down) under illumination with red, green, and blue light, resembling the potentiation behavior of biological synapse (Figure 4a−c). More importantly, it was found that the optoelectronic synapse could implement depression behavior by reversing the ferroelectric polarization in α-In$_2$Se$_3$ (positive weight control voltage, V_{GS} = 10 V, P up); the photocurrent gradually decreased under the illumination with 50 consecutive optical pulses. It should be noted that the decremental light response occurred at different wavelengths of the same optical frequency, achieving bidirectional synaptic weight update characteristics under optical pulse stimulation.

Different degrees of weight control voltage-configurable polarity on optoelectronic synapse performance were also

characterized, showing that the polarization state in α-In$_2$Se$_3$ influenced the extent to which photocurrent increased or decreased upon optical pulse stimulation (Figure S13). Furthermore, the tunable decreased photocurrent can be programmed by 50 consecutive pulses ranging from 0.5 to 1 Hz at different intensities, showing pulse frequency/intensity-dependent depression plasticity (Figure 4d and Figure S14). Particularly, the nonlinearity of potentiated and depressed synaptic weight updates is considered as the most critical characteristic in neuromorphic computing.[55,56] The detailed procedure for nonlinearity evaluation is presented in Figure S15. The LTP/D characteristics in the α-In$_2$Se$_3$ synaptic device were quantitatively evaluated by applying optical pulses under different weight control states (P down and P up) and fitting the nonlinearity from the LTP/D curves (Figure 4e,f, Figures
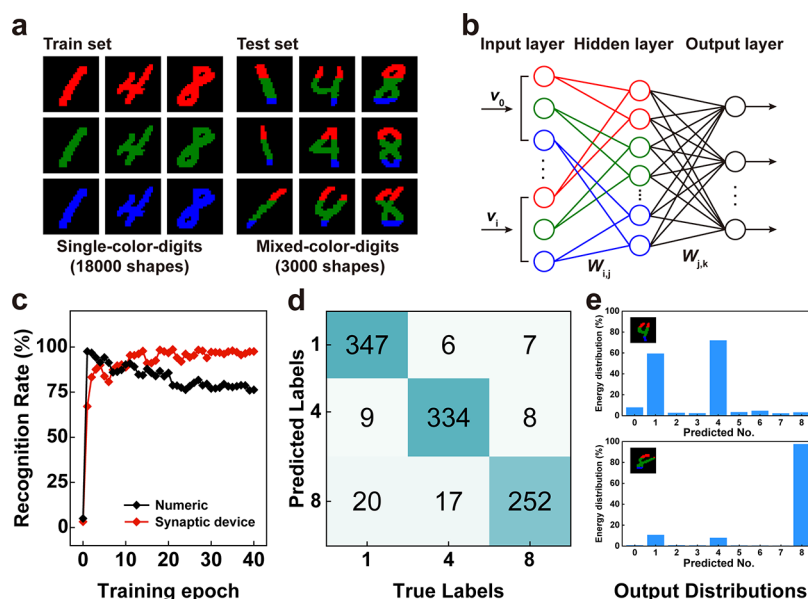
Figure 5. Implementation of α-In$_2$Se$_3$-based vision system for single and mixed color digits pattern recognition. (a) The single-color training data sets and mixed-color test data sets are developed for numbers of different shapes. (b) Schematic diagram of the neural network consisting of the input layer, hidden layer, and output layer. The input to the input layer is the feature of different digits. The output is the recognition result. We define nine output neurons to represent the output number. (c) Recognition accuracy as a function of training epochs on the developed test data set. (d) Confusion matrix of 1000 mixed-color digits used in our experiment. (e) The output intensity distribution of the neural network for digit numbers "4" and "8" is presented.

S16 & S17). The results reveal that the α-In$_2$Se$_3$ synaptic device achieved nearly linear weight update with a nonlinearity factor of $A_P = 0.52$ and $A_D = 1.20$, indicating the potential of this device for the development of high-performance neuromorphic computing hardware.

The multilevel current response after every 100 optical pulses was observed, showing the capability of continuous programming and retention characteristics in our device (Figure 4g). In addition, to assess the operational endurance of the device, the LTP and LTD characteristics were measured under an optical pulse stimulation for a total of 18 cycles (Figure 4h). The cycle-to-cycle variation (CCV) was calculated to be 6% and 3% for the LTP and LTD curves, respectively (Figure S18). These results demonstrate the device's outstanding performance in terms of operational reliability. A detailed comparison of other optoelectronic synaptic devices is presented in Table S1. The configurable potentiation and depression characteristics are achieved in our optoelectronic synapse under optical pulse stimulation, corresponding to the positive and negative synaptic weights in an artificial neural network, which is of great significance for neuromorphic computing.[57−61]

Mixed-Color Handwritten Pattern Classification. To demonstrate the feasibility of the α-In$_2$Se$_3$-based optoelectronic synapse for neuromorphic computing, the experimental synaptic weight update characteristics under optical pulse stimulation were used to carry out the colored and color-mixed data set recognition (training and inference) tasks. The pattern recognition tasks aim to identify target numbers from mixed-color test images where the target numbers are hidden in the mixed-color pattern. The Modified National Institute of Standards and Technology (MNIST) handwritten digits data set was used to provide the data sets for online learning neuromorphic tasks, while each digit image contained original size (28 × 28) and was appended with wavelength-dependent

color. We prepared a training data set with 18 000 shape patterns for single wavelength color numbers 1, 4, and 8 and a test data set with 3000 shape patterns for mixed-colored numbers (Figure 5a). As shown in Figure 5b, for MNIST and mixed-color MNIST digit classification, the designed fully connected neural network consists of an input layer with 784 neurons, a hidden layer with 300 neurons, an output layer with 300 neurons, and a synaptic weight (W) connecting them. The weight matrix size for the first layer was 784 × 300, and the weight matrix size for the second layer was 300 × 10 (including bias). The synaptic weight connections represent the measured conductance parameters of our optoelectronic synapse with LTP/LTD characteristics. After 40 epochs, the network recognition accuracy achieved by our experimental parameters reached 97% in the data set images, while the test accuracy using numeric weights showed a decremental trend and finally reached 76% (Figure 5c). Note that the accuracy of the numeric data decreased during training iteration, mainly due to the saturation of learning ability in the model. In contrast, the synaptic device achieved high accuracy with the same model, suggesting a significant learning capability under the premise of ensuring a number of parameters. It also means the potentiated and depressed synaptic weight updates of α-In$_2$Se$_3$ synaptic phototransistor have a negligible impact on the mixed-color pattern recognition accuracy.

Figure 5d presents the confusion matrix of the neural network, showing the classification effect by comparing the classification results with the true labels of the test data set, and the values on the diagonal of the confusion matrix are the number of times each digit was correctly classified. All three numbers were well-classified. The output distributions from nine predicted numbers for the classification of the digit "4" and "8" are depicted. The energy distribution percentage corresponding to each digit shows the maximum energy focused on the target label of the digit (Figure 5e). These

results demonstrated that the classification task could be successfully implemented based on our optoelectronic synaptic parameters. These results have demonstrated the potential of utilizing polarization switching in 2D ferroelectric semiconductors for hardware neural networks. However, the practical implementation of these prospects necessitates large-scale high-quality material growth and transfer techniques. Future practical applications of ferroelectric semiconductor devices will require higher integration density and the demonstration of learning and inference capabilities on hardware circuits (Figure S19).

CONCLUSION

In summary, a bidirectional synaptic phototransistor based on the ferroelectric semiconductor of α-In$_2$Se$_3$ was developed, with the synaptic weight potentiated and depressed *via* multiwavelength optical pulse stimulation. KPFM measurements were carried out to reveal the interlocked OOP-IP polarization switching under the gate modulation in a transistor structure. Utilizing the configurable barrier height variation, diverse synaptic characteristics, including PPF, STP/LTP, and LTD, as well as distinct bidirectional potentiated and depressed synaptic weight update *via* optical pulse stimulation, were demonstrated. Importantly, the emulation of the human vision system based on the α-In$_2$Se$_3$ synaptic phototransistor demonstrates the feasibility of both single-color and mixed-colored pattern recognition. These results provide opportunities to utilize polarization switching in 2D ferroelectric semiconductors for artificial vision systems.

EXPERIMENTAL METHODS

Device Fabrication. The p^{++} Si wafers were cleaned by sequential ultrasonication in the standard clean (SC-1) solution (1:2:7 NH$_4$OH/H$_2$O$_2$/H$_2$O at 55 °C) and deionized (DI) water for 10 min, then 30 nm-thick dielectric layer Al$_2$O$_3$ was grown by atomic layer deposition (ALD) in an SI ALD (SENTECH Instruments GmbH) at 170 °C in which trimethylaluminum precursors and water vapor were used as the oxidant. Subsequently, the α-In$_2$Se$_3$ flakes were mechanically exfoliated from bulk crystals (HQ Graphene, purity >99.995%) onto the Al$_2$O$_3$/Si substrate using Scotch tape (3M). The exfoliation was performed in the glovebox with a nitrogen environment. The devices had α-In$_2$Se$_3$ thickness range of 10−50 nm. For the field-effect transistor, the source/drain electrode patterns were defined by electron-beam lithography (EBL, Raith 150 Two) using a 200 nm thick 950K A4 poly(methyl methacrylate) (PMMA) resist. Then the electrode metal Cr/Au (5/50nm) was deposited by electron beam evaporation (High vacuum evaporation system ei-5z) and finally immersed in acetone for 10 min to lift-off; acetone can be heated to 50 °C for an easier lift-off operation.

Material Characterization. X-ray diffraction (XRD) was performed with Bruker D8 Advance technology to obtain crystallization information. The Raman measurement was performed on a WITec Alpha 300R Raman spectrometer (532 nm laser). The scanning electron microscopy (SEM) image was obtained by a Gemini500 (Zeiss) under a 10 kV electron beam. The transmission electron microscopy (TEM) images and X-ray energy-dispersive spectroscopy (EDS) were investigated by using an X-CFEG Spectra 300 (Thermo Fisher). Atomic force microscopy (AFM) and piezoelectric force microscopy (PFM) measurements of the α-In$_2$Se$_3$ were performed using a commercial instrument (Cypher ES, Oxford); α-In$_2$Se$_3$ flakes were transferred on Au (30 nm)/Si substrate using Ti/Pt (5/20 nm)-coated conductive tips (AC240TM, Olympus). The out-of-plane and in-plane piezoelectric signals were investigated at a contact resonance frequency of ~280 kHz in dual-ac resonance tracking (DART) PFM mode. Contact potential difference (CPD) images and signals of the as-prepared device (channel length:

1 μm) were carried out in amplitude-modulated Kelvin probe force microscopy (AM-KPFM) (Dimension Icon, Bruker) under an ambient atmosphere, and Pt/Ir-coated Si tips (SCM-PIT-V2, Bruker) were used. During the measurements, the lift mode was used with a lift scan height of 40 nm regarding the signal-to-noise ratio. A source meter (Keysight 2912B) was used to apply an electric field. During the measurements, CPD is created between a tip and the device surface, which can be used to quantify the work function (WF) via equation 1

$$V_{\text{CPD}} = \frac{W_{\text{tip}} - W_{\text{sample}}}{e^-} \tag{1}$$

where φ_{tip} is the WF of the tip, and φ_{sample} is the WF of the sample surface.

Electrical Characterization. The channel width (W) and length (L) of the resulting devices for electrical characterization were about 8 μm and 500 nm unless otherwise specified. The electrical properties were measured by using a semiconductor parameter analyzer (Keithley 4200 SCS) at room temperature under ambient conditions.

The effect of paired-pulse facilitation (PPF), a specific case of fundamental synaptic behavior, was demonstrated by applying two consecutive optical pulses. The PPF index is defined by the ratio of A_2/A_1 and can be simulated by equation 2

$$\text{PPF index} = \frac{A_2}{A_1} = 1 + C_1 \exp\left(-\frac{\Delta t}{\tau_1}\right) + C_2 \exp\left(-\frac{\Delta t}{\tau_2}\right) \tag{2}$$

where Δt is the optical pulse interval, A_1 and A_2 represent the peak amplitudes of current evoked by the first and second optical pulses, C_1 and C_2 are the initial facilitation magnitudes of the rapid and slow phases, and τ_1 and τ_2 are the relaxation time of the rapid and slow phases, respectively.[15]

ASSOCIATED CONTENT

Ⓢ Supporting Information

The Supporting Information is available free of charge at https://pubs.acs.org/doi/10.1021/acsnano.3c02167.

The material characterization of $2H$ α-In$_2$Se$_3$, piezoelectric force microscopy (PFM) characterization, transfer characteristics of the α-In$_2$Se$_3$-based devices, output characteristic of the synaptic phototransistor, the schematic of Kevin probe force measurement (KPFM), photograph of the KPFM measurement of the as-prepared device with *in situ* AFM electrical nanotechnology, the KPFM measurement of the α-In$_2$Se$_3$ synaptic phototransistor, the KPFM measurement of the device under different bias, the lock-in polarization of α-In$_2$Se$_3$, optical-stimulated synaptic characteristics at a wavelength of 520 nm (green) and 450 nm (blue), fitting the photocurrent decay process after an optical pulse, optical-stimulated synaptic characteristics under different polarities, optical-stimulated synaptic characteristics under different intensities and frequencies, nonlinear weight update model of potentiation (P) and depression (D) characteristics curves, nonlinear weight update analysis of LTP/LTD curves, cycle-to-cycle variation (CCV) of the synaptic device, and the α-In$_2$Se$_3$-based synaptic device for the conceptual neural networks. A supplementary table illustrating performance benchmark of our optoelectronic synapse in comparison with other synaptic devices (PDF)

AUTHOR INFORMATION

Corresponding Author

Bowen Zhu − *Key Laboratory of 3D Micro/Nano Fabrication and Characterization of Zhejiang Province, School of Engineering, Westlake University, Hangzhou 310024, China; Institute of Advanced Technology, Westlake Institute for Advanced Study, Hangzhou 310024, China;* orcid.org/0000-0001-7534-9723; Email: zhubowen@westlake.edu.cn

Authors

Yitong Chen − *School of Materials Science and Engineering, Zhejiang University, Hangzhou 310027, China; Key Laboratory of 3D Micro/Nano Fabrication and Characterization of Zhejiang Province, School of Engineering, Westlake University, Hangzhou 310024, China*

Min Zhang − *School of Engineering, Westlake University, Hangzhou 310024, China*

Dingwei Li − *Key Laboratory of 3D Micro/Nano Fabrication and Characterization of Zhejiang Province, School of Engineering, Westlake University, Hangzhou 310024, China*

Yingjie Tang − *Key Laboratory of 3D Micro/Nano Fabrication and Characterization of Zhejiang Province, School of Engineering, Westlake University, Hangzhou 310024, China*

Huihui Ren − *School of Materials Science and Engineering, Zhejiang University, Hangzhou 310027, China; Key Laboratory of 3D Micro/Nano Fabrication and Characterization of Zhejiang Province, School of Engineering, Westlake University, Hangzhou 310024, China*

Jiye Li − *School of Materials Science and Engineering, Zhejiang University, Hangzhou 310027, China; Key Laboratory of 3D Micro/Nano Fabrication and Characterization of Zhejiang Province, School of Engineering, Westlake University, Hangzhou 310024, China*

Kun Liang − *Key Laboratory of 3D Micro/Nano Fabrication and Characterization of Zhejiang Province, School of Engineering, Westlake University, Hangzhou 310024, China*

Yan Wang − *Key Laboratory of 3D Micro/Nano Fabrication and Characterization of Zhejiang Province, School of Engineering, Westlake University, Hangzhou 310024, China;* orcid.org/0000-0002-6997-6779

Liaoyong Wen − *Key Laboratory of 3D Micro/Nano Fabrication and Characterization of Zhejiang Province, School of Engineering, Westlake University, Hangzhou 310024, China;* orcid.org/0000-0003-3185-575X

Wenbin Li − *Key Laboratory of 3D Micro/Nano Fabrication and Characterization of Zhejiang Province, School of Engineering, Westlake University, Hangzhou 310024, China;* orcid.org/0000-0002-1240-2707

Wei Kong − *Key Laboratory of 3D Micro/Nano Fabrication and Characterization of Zhejiang Province, School of Engineering, Westlake University, Hangzhou 310024, China*

Shi Liu − *School of Science, Westlake University, Hangzhou 310024 Zhejiang, China;* orcid.org/0000-0002-8488-4848

Hong Wang − *Key Laboratory of Wide Band Gap Semiconductor Technology, School of Microelectronics Xidian University, Xi'an 710071, China;* orcid.org/0000-0002-0213-3523

Donglin Wang − *School of Engineering, Westlake University, Hangzhou 310024, China*

Complete contact information is available at:

Author Contributions

All authors participated in the scientific discussion. B.Z. conceived the project and supervised the overall research. Y.C. conducted most of the experiments and analyzed the data. M.Z. performed the simulation. H.R. conducted the XRD experiment. D.L., Y.T., H.R., J.L., K.L., Y.W., L.W., W.L., W.K., S.L., H.W., and D.W. contributed to material characterizations, device fabrications, or data analysis. Y.C. and B.Z. wrote the manuscript.

Notes

The authors declare no competing financial interest.

REFERENCES

(1) Roy, K.; Jaiswal, A.; Panda, P. Towards spike-based machine intelligence with neuromorphic computing. *Nature* **2019**, *575*, 607−617.

(2) Zhang, W.; Gao, B.; Tang, J.; Yao, P.; Yu, S.; Chang, M.-F.; Yoo, H.-J.; Qian, H.; Wu, H. Neuro-inspired computing chips. *Nat. Electron.* **2020**, *3*, 371−382.

(3) Marković, D.; Mizrahi, A.; Querlioz, D.; Grollier, J. Physics for neuromorphic computing. *Nat. Rev. Phys.* **2020**, *2*, 499−510.

(4) Beck, M. E.; Hersam, M. C. Emerging opportunities for electrostatic control in atomically thin devices. *ACS Nano* **2020**, *14*, 6498−6518.

(5) Cho, S. W.; Kwon, S. M.; Kim, Y.-H.; Park, S. K. Recent progress in transistor-based optoelectronic synapses: From neuromorphic computing to artificial sensory system. *Adv. Intell. Syst.* **2021**, *3*, 2000162.

(6) Han, X.; Xu, Z.; Wu, W.; Liu, X.; Yan, P.; Pan, C. Recent progress in optoelectronic synapses for artificial visual-perception system. *Small Struct.* **2020**, *1*, 2000029.

(7) Zhang, J.; Dai, S.; Zhao, Y.; Zhang, J.; Huang, J. Recent progress in photonic synapses for neuromorphic systems. *Adv. Intell. Syst.* **2020**, *2*, 1900136.

(8) Cheng, Z.; Ríos, C.; Pernice, W. H. P.; Wright, C. D.; Bhaskaran, H. On-chip photonic synapse. *Sci. Adv.* **2017**, *3*, e1700160.

(9) He, K.; Liu, Y.; Yu, J.; Guo, X.; Wang, M.; Zhang, L.; Wan, C.; Wang, T.; Zhou, C.; Chen, X. Artificial neural pathway based on a memristor synapse for optically mediated motion learning. *ACS Nano* **2022**, *16*, 9691−9700.

(10) Cho, S. W.; Jo, C.; Kim, Y. H.; Park, S. K. Progress of materials and devices for neuromorphic vision sensors. *Nanomicro Lett.* **2022**, *14*, 203.

(11) Seung, H.; Choi, C.; Kim, D. C.; Kim, J. S.; Kim, J. H.; Kim, J.; Park, S. I.; Lim, J. A.; Yang, J.; Choi, M. K.; et al. Integration of synaptic phototransistors and quantum dot light-emitting diodes for visualization and recognition of uv patterns. *Sci. Adv.* **2022**, *8*, eabq3101.

(12) Wang, J.; Wang, C.; Cai, P.; Luo, Y.; Cui, Z.; Loh, X. J.; Chen, X. Artificial sense technology: Emulating and extending biological senses. *ACS Nano* **2021**, *15*, 18671−18678.

(13) Wang, S. Y.; Chen, C. S.; Yu, Z. H.; He, Y. L.; Chen, X. Y.; Wan, Q.; Shi, Y.; Zhang, D. W.; Zhou, H.; Wang, X. R.; et al. A MoS_2/PTCDA hybrid heterojunction synapse with efficient photoelectric dual modulation and versatility. *Adv. Mater.* **2019**, *31*, 1806227.

(14) Kwon, S. M.; Cho, S. W.; Kim, M.; Heo, J. S.; Kim, Y. H.; Park, S. K. Environment-adaptable artificial visual perception behaviors using a light-adjustable optoelectronic neuromorphic device array. *Adv. Mater.* **2019**, *31*, 1906433.

(15) Liang, K.; Wang, R.; Huo, B.; Ren, H.; Li, D.; Wang, Y.; Tang, Y.; Chen, Y.; Song, C.; Li, F.; et al. Fully printed optoelectronic synaptic transistors based on quantum dot-metal oxide semiconductor heterojunctions. *ACS Nano* **2022**, *16*, 8651−8661.

(16) Luo, Z. D.; Xia, X.; Yang, M. M.; Wilson, N. R.; Gruverman, A.; Alexe, M. Artificial optoelectronic synapses based on ferroelectric field-effect enabled 2D transition metal dichalcogenide memristive transistors. *ACS Nano* **2020**, *14*, 746−754.

(17) Portner, K.; Schmuck, M.; Lehmann, P.; Weilenmann, C.; Haffner, C.; Ma, P.; Leuthold, J.; Luisier, M.; Emboras, A. Analog nanoscale electro-optical synapses for neuromorphic computing applications. *ACS Nano* **2021**, *15*, 14776−14785.

(18) Ahmed, T.; Kuriakose, S.; Mayes, E. L. H.; Ramanathan, R.; Bansal, V.; Bhaskaran, M.; Sriram, S.; Walia, S. Optically stimulated artificial synapse based on layered black phosphorus. *Small* **2019**, *15*, 1900966.

(19) Ahmed, T.; Kuriakose, S.; Abbas, S.; Spencer, M. J. S.; Rahman, M. A.; Tahir, M.; Lu, Y.; Sonar, P.; Bansal, V.; Bhaskaran, M.; et al. Multifunctional optoelectronics via harnessing defects in layered black phosphorus. *Adv. Funct. Mater.* **2019**, *29*, 1901991.

(20) Ahmed, T.; Tahir, M.; Low, M. X.; Ren, Y.; Tawfik, S. A.; Mayes, E. L. H.; Kuriakose, S.; Nawaz, S.; Spencer, M. J. S.; Chen, H.; et al. Fully light-controlled memory and neuromorphic computation in layered black phosphorus. *Adv. Mater.* **2021**, *33*, 2004207.

(21) Ryder, C. R.; Wood, J. D.; Wells, S. A.; Hersam, M. C. Chemically tailoring semiconducting two-dimensional transition metal dichalcogenides and black phosphorus. *ACS Nano* **2016**, *10*, 3900−3917.

(22) Seo, S.; Jo, S. H.; Kim, S.; Shim, J.; Oh, S.; Kim, J. H.; Heo, K.; Choi, J. W.; Choi, C.; Oh, S.; et al. Artificial optic-neural synapse for colored and color-mixed pattern recognition. *Nat. Commun.* **2018**, *9*, 5106.

(23) Hu, L.; Yang, J.; Wang, J.; Cheng, P.; Chua, L. O.; Zhuge, F. All-optically controlled memristor for optoelectronic neuromorphic computing. *Adv. Funct. Mater.* **2021**, *31*, 2005582.

(24) Hong, X.; Huang, Y.; Tian, Q.; Zhang, S.; Liu, C.; Wang, L.; Zhang, K.; Sun, J.; Liao, L.; Zou, X. Two-dimensional perovskite-gated AlGAN/GAN high-electron-mobility-transistor for neuromorphic vision sensor. *Adv. Sci.* **2022**, *9*, 2202019.

(25) Wang, Y.; Zhu, Y.; Li, Y.; Zhang, Y.; Yang, D.; Pi, X. Dual-modal optoelectronic synaptic devices with versatile synaptic plasticity. *Adv. Funct. Mater.* **2022**, *32*, 2107973.

(26) Yang, C. M.; Chen, T. C.; Verma, D.; Li, L. J.; Liu, B.; Chang, W. H.; Lai, C. S. Bidirectional all-optical synapses based on a 2D Bi_2O_2Se/graphene hybrid structure for multifunctional optoelectronics. *Adv. Funct. Mater.* **2020**, *30*, 2001598.

(27) Huang, X.; Li, Q.; Shi, W.; Liu, K.; Zhang, Y.; Liu, Y.; Wei, X.; Zhao, Z.; Guo, Y.; Liu, Y. Dual-mode learning of ambipolar synaptic phototransistor based on 2D perovskite/organic heterojunction for flexible color recognizable visual system. *Small* **2021**, *17*, 2102820.

(28) Li, H.; Jiang, X.; Ye, W.; Zhang, H.; Zhou, L.; Zhang, F.; She, D.; Zhou, Y.; Han, S.-T. Fully photon modulated heterostructure for neuromorphic computing. *Nano Energy* **2019**, *65*, 104000.

(29) Li, D.; Chen, Y.; Tang, Y.; Liang, K.; Ren, H.; Li, F.; Wang, Y.; Liu, G.; Song, C.; Meng, L. Solution-processed organic−inorganic semiconductor heterostructures for advanced hybrid phototransistors. *ACS Appl. Electron. Mater.* **2023**, *5*, 578.

(30) Si, M.; Saha, A. K.; Gao, S.; Qiu, G.; Qin, J.; Duan, Y.; Jian, J.; Niu, C.; Wang, H.; Wu, W.; et al. A ferroelectric semiconductor field-effect transistor. *Nat. Electron.* **2019**, *2* (12), 580−586.

(31) Wang, S.; Liu, L.; Gan, L.; Chen, H.; Hou, X.; Ding, Y.; Ma, S.; Zhang, D. W.; Zhou, P. Two-dimensional ferroelectric channel transistors integrating ultra-fast memory and neural computing. *Nat. Commun.* **2021**, *12*, 53.

(32) Chen, Y.; Li, D.; Ren, H.; Tang, Y.; Liang, K.; Wang, Y.; Li, F.; Song, C.; Guan, J.; Chen, Z.; et al. Highly linear and symmetric synaptic memtransistors based on polarization switching in two-dimensional ferroelectric semiconductors. *Small* **2022**, 2203611.

(33) Zheng, X.; Han, W.; Yang, K.; Wong, L. W.; Tsang, C. S.; Lai, K. H.; Zheng, F.; Yang, T.; Lau, S. P.; Ly, T. H.; et al. Phase and polarization modulation in two-dimensional In_2Se_3 via in situ transmission electron microscopy. *Sci. Adv.* **2022**, *8*, eabo0773.

(34) Han, W.; Zheng, X.; Yang, K.; Tsang, C. S.; Zheng, F.; Wong, L. W.; Lai, K. H.; Yang, T.; Wei, Q.; Li, M.; et al. Phase-controllable large-area two-dimensional In_2Se_3 and ferroelectric heterophase junction. *Nat. Nanotechnol.* **2023**, *18*, 55−63.

(35) Sangwan, V. K.; Liu, S. E.; Trivedi, A. R.; Hersam, M. C. Two-dimensional materials for bio-realistic neuronal computing networks. *Matter* **2022**, *5*, 4133−4152.

(36) Li, J.; Li, H.; Niu, X.; Wang, Z. Low-dimensional In_2Se_3 compounds: From material preparations to device applications. *ACS Nano* **2021**, *15*, 18683−18707.

(37) Jia, C.; Wu, S.; Fan, J.; Luo, C.; Fan, M.; Li, M.; He, L.; Yang, Y.; Zhang, H. Ferroelectrically modulated and enhanced photo-response in a self-powered alpha-In_2Se_3/Si heterojunction photo-detector. *ACS Nano* **2023**, *17*, 6534.

(38) Yang, J. Y.; Park, M.; Yeom, M. J.; Baek, Y.; Yoon, S. C.; Jeong, Y. J.; Oh, S. Y.; Lee, K.; Yoo, G. Reconfigurable physical reservoir in GaN/alpha-In_2Se_3 hemts enabled by out-of-plane local polarization of ferroelectric 2D layer. *ACS Nano* **2023**, *17*, 7695.

(39) Liu, K.; Zhang, T.; Dang, B.; Bao, L.; Xu, L.; Cheng, C.; Yang, Z.; Huang, R.; Yang, Y. An optoelectronic synapse based on α-In_2Se_3 with controllable temporal dynamics for multimode and multiscale reservoir computing. *Nat. Electron.* **2022**, *5*, 761−773.

(40) Xue, F.; He, X.; Liu, W.; Periyanagounder, D.; Zhang, C.; Chen, M.; Lin, C. H.; Luo, L.; Yengel, E.; Tung, V.; et al. Optoelectronic ferroelectric domain-wall memories made from a single van der waals ferroelectric. *Adv. Funct. Mater.* **2020**, *30*, 2004206.

(41) Jin, T.; Mao, J.; Gao, J.; Han, C.; Loh, K. P.; Wee, A. T. S.; Chen, W. Ferroelectrics-integrated two-dimensional devices toward next-generation electronics. *ACS Nano* **2022**, *16*, 13595−13611.

(42) Zhou, Y.; Wu, D.; Zhu, Y.; Cho, Y.; He, Q.; Yang, X.; Herrera, K.; Chu, Z.; Han, Y.; Downer, M. C.; et al. Out-of-plane piezoelectricity and ferroelectricity in layered alpha-In_2Se_3 nanoflakes. *Nano Lett.* **2017**, *17*, 5508−5513.

(43) Xue, F.; He, X.; Retamal, J. R. D.; Han, A.; Zhang, J.; Liu, Z.; Huang, J. K.; Hu, W.; Tung, V.; He, J. H.; et al. Gate-tunable and multidirection-switchable memristive phenomena in a van der waals ferroelectric. *Adv. Mater.* **2019**, *31*, 1901300.

(44) Xue, F.; He, X.; Wang, Z.; Retamal, J. R. D.; Chai, Z.; Jing, L.; Zhang, C.; Fang, H.; Chai, Y.; Jiang, T.; et al. Giant ferroelectric resistance switching controlled by a modulatory terminal for low-power neuromorphic in-memory computing. *Adv. Mater.* **2021**, *33*, 2008709.

(45) Liu, K.; Dang, B.; Zhang, T.; Yang, Z.; Bao, L.; Xu, L.; Cheng, C.; Huang, R.; Yang, Y. Multilayer reservoir computing based on ferroelectric alpha-In_2Se_3 for hierarchical information processing. *Adv. Mater.* **2022**, 2108826.

(46) Si, M.; Zhang, Z.; Chang, S. C.; Haratipour, N.; Zheng, D.; Li, J.; Avci, U. E.; Ye, P. D. Asymmetric metal/alpha-In_2Se_3/Si crossbar ferroelectric semiconductor junction. *ACS Nano* **2021**, *15*, 5689−5695.

(47) Xue, F.; Zhang, J.; Hu, W.; Hsu, W. T.; Han, A.; Leung, S. F.; Huang, J. K.; Wan, Y.; Liu, S.; Zhang, J.; et al. Multidirection piezoelectricity in mono- and multilayered hexagonal α- In_2Se_3. *ACS Nano* **2018**, *12*, 4976−4983.

(48) Huang, Y. T.; Chen, N. K.; Li, Z. Z.; Wang, X. P.; Sun, H. B.; Zhang, S.; Li, X. B. Two-dimensional In$_2$Se$_3$: A rising advanced material for ferroelectric data storage. *Infomat* **2022**, *4*, 12341.

(49) Xiao, J.; Zhu, H.; Wang, Y.; Feng, W.; Hu, Y.; Dasgupta, A.; Han, Y.; Wang, Y.; Muller, D. A.; Martin, L. W.; et al. Intrinsic two-dimensional ferroelectricity with dipole locking. *Phys. Rev. Lett.* **2018**, *120*, 227601.

(50) Han, G.; Chen, Z. G.; Drennan, J.; Zou, J. Indium selenides: Structural characteristics, synthesis and their thermoelectric performances. *Small* **2014**, *10*, 2747−2765.

(51) Gruverman, A.; Alexe, M.; Meier, D. Piezoresponse force microscopy and nanoferroic phenomena. *Nat. Commun.* **2019**, *10*, 1661.

(52) Zhang, H. Y.; Chen, X. G.; Tang, Y. Y.; Liao, W. Q.; Di, F. F.; Mu, X.; Peng, H.; Xiong, R. G. PFM (piezoresponse force microscopy)-aided design for molecular ferroelectrics. *Chem. Soc. Rev.* **2021**, *50*, 8248−8278.

(53) Melitz, W.; Shen, J.; Kummel, A. C.; Lee, S. Kelvin probe force microscopy and its application. *Sur. Sci. Rep.* **2011**, *66*, 1−27.

(54) Wang, Y.; Lv, Z.; Chen, J.; Wang, Z.; Zhou, Y.; Zhou, L.; Chen, X.; Han, S. T. Photonic synapses based on inorganic perovskite quantum dots for neuromorphic computing. *Adv. Mater.* **2018**, *30*, 1802883.

(55) Chen, P. Y.; Peng, X.; Yu, S. Neurosim+: An integrated device-to-algorithm framework for benchmarking synaptic devices and array architectures. In *2017 IEEE International Electron Devices Meeting (IEDM)*, San Francisco, CA, 2017; IEEE, 2017, 6.1.1−6.1.4. DOI: 10.1109/IEDM.2017.8268337

(56) Yu, S. Neuro-inspired computing with emerging nonvolatile memorys. *Proceedings of the IEEE* **2018**, *106*, 260−285.

(57) Wan, T.; Shao, B.; Ma, S.; Zhou, Y.; Li, Q.; Chai, Y. In-sensor computing: Materials, devices, and integration technologies. *Adv. Mater.* **2022**, 2203830.

(58) Shim, H.; Sim, K.; Ershad, F.; Yang, P.; Thukral, A.; Rao, Z.; Kim, H.-J.; Liu, Y.; Wang, X.; Gu, G.; et al. Stretchable elastic synaptic transistors for neurologically integrated soft engineering systems. *Sci. Adv.* **2019**, *5*, eaax4961.

(59) Shim, H.; Jang, S.; Jang, J. G.; Rao, Z.; Hong, J.-I.; Sim, K.; Yu, C. Fully rubbery synaptic transistors made out of all-organic materials for elastic neurological electronic skin. *Nano Res.* **2022**, *15*, 758−764.

(60) Shim, H.; Jang, S.; Thukral, A.; Jeong, S.; Jo, H.; Kan, B.; Patel, S.; Wei, G.; Lan, W.; Kim, H. J.; et al. Artificial neuromorphic cognitive skins based on distributed biaxially stretchable elastomeric synaptic transistors. *Proc. Natl. Acad. Sci. USA* **2022**, *119*, e2204852119.

(61) Shim, H.; Ershad, F.; Patel, S.; Zhang, Y. C.; Wang, B. H.; Chen, Z. H.; Marks, T. J.; Facchetti, A.; Yu, C. J. An elastic and reconfigurable synaptic transistor based on a stretchable bilayer semiconductor. *Nat. Electron.* **2022**, *5*, 660−671.